Folding Simulation of Elastically Foldable Flat Arrays Using Refined Beam Finite Elements

R. Augello* and E. Carrera †
Politecnico di Torino, Torino, Italy, 10129.

Sergio Pellegrino‡
California Institute of Technology, Pasadena, CA, 91125

This work explores the numerical simulation of the folding of complex structures consisting of pairs of Triangular Rollable and Collapsible (TRAC) longerons linked by transverse battens and parallel hinges. The analysis uses the Carrera Unified Formulation (CUF), which divides the three-dimensional displacement field of the structure into axial and cross-sectional terms, enabling one-dimensional beam finite elements to be used without sacrificing accuracy. Higher-order CUF models capture cross-sectional deformation through nine-point Lagrange expansions, extending through the whole structure. Thus, the numerical model of a complete structure consists of a single beam. An implicit quasi-static scheme, coupling Newton–Raphson iterations with displacement control is used across all analyses. Contact between the longerons is represented by nonlinear spring elements assigned to prescribed pairs of nodes.

Nomenclature

b_l	=	linear differential operator
b_{nl}	=	nonlinear differential operator
$\mathbf{C}$	=	stiffness matrix for linear elastic material
F_τ	=	expansion functions along thickness coordinate z
$\mathbf{K}_S^{ij\tau s}$	=	fundamental nucleus of secant stiffness matrix
$\mathbf{K}_T^{ij\tau s}$	=	fundamental nucleus of tangent stiffness matrix
$\mathbf{L}_{ine}$	=	work of inertial loads
$\mathbf{L}_{ext}$	=	work of external loads
$\mathbf{L}_{int}$	=	strain energy
M	=	number of terms in expansion in cross-section plane

*Postdoc, Politecnico di Torino, Torino, Italy, 10129. AIAA Young Professional. E-mail: riccardo.augello@polito.it.
†Professor, Politecnico di Torino, Torino, Italy, 10129. E-mail: erasmo.carrera@polito.it.
‡Joyce and Kent Kresa Professor of Aerospace and Civil Engineering; Jet Propulsion Laboratory Senior Research Scientist; Co-Director, Space-Based Solar Power Project, Graduate Aerospace Laboratories, MC 105-50. California Institute of Technology, Pasadena, CA, 91125. AIAA Fellow. E-mail: sergiop@caltech.edu

N_i = shape function

N_n = number of finite element nodes per element

$\mathbf{u}_\tau, \mathbf{u}_{\tau i}$ = generalized displacement vector and finite element nodal parameters

δ = variation

$\boldsymbol{\epsilon}$ = strain vector

$\boldsymbol{\sigma}$ = stress vector

I. Introduction

Lightweight deployable structures have emerged as a key enabling technology to reconcile the need for large functional surfaces with the volume and mass constraints imposed by modern launch vehicles. In parallel with the trend towards more capable spacecraft, deployable booms and frames are increasingly used to support antennas, solar arrays, telescopes and other large appendages that have to be folded to allow stowage for launch [1].

The simplest and most widespread of these structures is the tape spring, a thin elastic strip that can be elastically coiled and then deployed into a straight beam. The introduction of carbon-fibre-reinforced plastic (CFRP) tape springs has further improved stiffness-to-mass ratios and thermal stability, making them particularly attractive for high-performance space structures [2]. To enhance the bending stiffness, load-carrying capability and packaging efficiency, alternative cross-sectional layouts have been proposed. A prominent example is the Triangular Rollable and Collapsible (TRAC) boom, originally developed at the Air Force Research Laboratory [3, 4]. TRAC booms combine two tape-spring-like circular arcs (flanges) connected along a shared edge (web), forming a closed or semi-closed triangular cross-section with markedly superior bending stiffness compared to single tape springs. Metallic TRAC booms were successfully flown, for instance, in NASA's NanoSail-D solar sail demonstrator [5], whereas more recent developments have focused on composite beams to mitigate thermal-gradient issues experienced by metallic booms in sail applications. Rollable TRAC and tape-spring booms have also been adopted in deployable telescopes and similar large-aperture systems [6].

An application of particular interest for these structures is the Caltech Space Solar Power Project (SSPP), which aims at collecting solar energy in space and transmitting it wirelessly to Earth. The SSPP concept is based on a modular, ultralight deployable structure that acts as a frame supporting multifunctional tiles integrating photovoltaic conversion and radio-frequency (RF) transmission hardware [7]. The structural backbone of each module is a set of bending-stiff trapezoidal strips arranged in four identical quadrants. The two edges of each strip are formed by composite TRAC longerons, interconnected by CFRP battens and tensioned membranes. In such architectures, the dynamic performance of the longerons is critical, as it directly affects pointing accuracy, structural robustness and the overall efficiency of the power transmission system.

Because of their slenderness, thin-walled construction and ultra-light mass, deployable booms and frames are inherently

susceptible to dynamic excitations. Low inherent damping can lead to significant vibration amplification under launch loads, on-orbit maneuvers or operational perturbations [8]. In addition, large quasi-static deformations – for instance those induced during deployment, folding, or under membrane-induced loads – can drive the structure into regimes where geometric nonlinearity dominates the response [9, 10]. Under such conditions, localized nonlinear phenomena, including local buckling, snap-through and mode interaction, may arise within the cross-section or along the span [11, 12]. These local events can, in turn, strongly modify the global dynamic behavior, altering natural frequencies, mode shapes and vibration attenuation mechanisms in ways that are not captured by linear models [13].

Numerical methods based on the Finite Element Method (FEM) are the primary tools used to study deployable longerons and frameworks. However, conventional FEM discretizations face multiple challenges. The extreme slenderness and thin walls of the longerons often necessitate two-dimensional (2D) shell or even three-dimensional (3D) solid elements to correctly capture cross-sectional warping, local buckling and out-of-plane features, particularly in anisotropic composite laminates [14]. This requirement leads to very fine meshes and high computational costs, especially when large-displacement geometric nonlinearities and time-dependent loads must be resolved.

To overcome these limitations, this work adopts a finite element framework based on the Carrera Unified Formulation (CUF) [15]. CUF enriches one-dimensional (1D) beam elements with three-dimensional capabilities by expanding the cross-sectional displacement field through hierarchical, higher-order functions. In this way, detailed cross-sectional deformations – including local buckling modes and warping – can be represented within a 1D kinematic description. The formulation is derived from the full three-dimensional Green–Lagrange strain tensor and associated nonlinear governing equations, allowing geometric nonlinearities to be consistently included without ad hoc assumptions [16]. Compared with conventional 2D/3D FE models, CUF-based 1D elements offer a drastic reduction in the number of degrees of freedom while retaining the accuracy required to capture local and global effects in slender composite members.

Recent applications have demonstrated the effectiveness of CUF for deployable boom analysis. Detailed numerical investigations have been carried out on the buckling and post-buckling behavior of TRAC-like composite booms, showing that CUF models can accurately reproduce complex localization patterns and load–displacement paths with a modest computational effort [17, 18]. More recently, CUF-based formulations have been employed to study the folding of complete TRAC longerons and flat deployable arrays, capturing both the global kinematics and the local strain distributions that govern durability and damage initiation [19]. These studies, however, have mainly focused on static or quasi-static loading conditions. The present work builds on these advances and extends the CUF framework to the nonlinear analysis of composite TRAC longerons representative of those used in SSPP-like architectures. The focus is on the rotation and folding of the structure.

II. Refined one-dimensional finite element formulation

The basic structure analyzed in this work is the foldable Triangular Rollable and Collapsible (TRAC) longeron shown in Fig. 1. The cross-section consists of two curved regions, referred to as flanges, connected by a straight portion, referred to as the web. For the development of the numerical model, a Cartesian reference system is adopted.

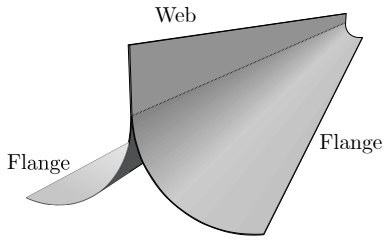

Fig. 1 TRAC longeron. The curved domains are the flanges, the straight domain is the web.

The y-axis coincides with the boom axis (length direction), whereas the coordinates x and z span the cross-sectional domain, as schematically illustrated in Fig. 2. Within the framework of the Carrera Unified Formulation (CUF), the

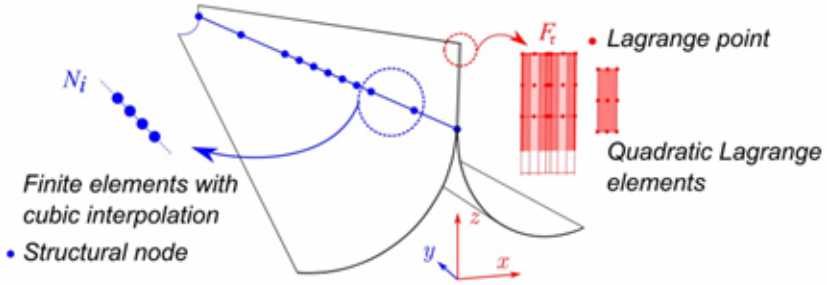

Fig. 2 CUF-based model of TRAC longeron.

three-dimensional displacement field and its virtual variation are expressed in the unified form

$$\begin{aligned} \mathbf{u}(x,y,z) &= F_\tau(x,z)\mathbf{u}_\tau(y), \quad \tau = 1,2,...,M \\ \delta\mathbf{u}(x,y,z) &= F_s(x,z)\delta\mathbf{u}_s(y), \quad s = 1,2,...,M \end{aligned} \tag{1}$$

where $F\tau$ and F_s are cross-sectional expansion functions depending on the coordinates x and z, τ and s are summation indices, and M denotes the number of terms used in the cross-sectional expansion. In the present work, quadratic Lagrange polynomials with nine nodes (L9) are adopted as F_τ to approximate the cross-sectional kinematics. This choice allows higher-order models to be implemented in a straightforward manner (see Carrera and Petrolo [20] for further details).

As an example, the displacement field associated with a single L9 polynomial expansion is quadratic in x and z and

can be written as

$$\begin{aligned} u_x(x,y,z) &= F_1(x,z)u_{x_1}(y) + F_2(x,z)u_{x_2}(y) + \cdots + F_9(x,z)u_{x_9}(y), \\ u_y(x,y,z) &= F_1(x,z)u_{y_1}(y) + F_2(x,z)u_{y_2}(y) + \cdots + F_9(x,z)u_{y_9}(y), \\ uz(x,y,z) &= F_1(x,z)u_{z_1}(y) + F_2(x,z)u_{z_2}(y) + \cdots + F_9(x,z)u_{z_9}(y), \end{aligned} \tag{2}$$

where $u_{x_1}, \ldots, u_{x_9}, u_{y_1}, \ldots, u_{y_9}$ and $u_{z_1}, \ldots, uz9$ are the displacement components at the nine cross-sectional Lagrange points, and $F_1, \ldots, F_9$ are the associated Lagrange shape functions in the (x, z) plane. Further details on the Lagrange expansion can be found in [21].

To approximate the displacement field along the beam axis, the Finite Element Method (FEM) is employed. The generalized displacement vectors $\mathbf{u}_\tau(y)$ and their virtual variations $\delta\mathbf{u}_{s(y)}$ are interpolated as

$$\begin{aligned} \mathbf{u}_\tau(y) &= N_i(y)\mathbf{u}_{\tau i}, \quad i = 1, 2, \ldots, N_n \\ \delta\mathbf{u}_s(y) &= N_j(y)\delta\mathbf{u}_{sj}, \quad j = 1, 2, \ldots, N_n \end{aligned} \tag{3}$$

where N_i and N_j denote the one-dimensional shape functions along the y-axis, i and j are summation indices, and N_n is the number of nodes per finite element. In this work, both linear (B2) and cubic (B4) beam elements are considered. The vectors of nodal unknowns and virtual nodal values are written as

$$\begin{aligned} \mathbf{u}_{\tau i} &= \{\mathbf{u}_{x_{\tau i}}\ \mathbf{u}_{y_{\tau i}}\ \mathbf{u}_{z_{\tau i}}\}^T \\ \delta\mathbf{u}_{sj} &= \{\delta\mathbf{u}_{x_{sj}}\ \delta\mathbf{u}_{y_{sj}}\ \delta\mathbf{u}_{z_{sj}}\}^T \end{aligned} \tag{4}$$

In the numerical applications discussed in this work, classical one-dimensional Lagrangian finite elements with four nodes (B4) are primarily used, providing cubic interpolation along the y-direction [22]. Figure 2 illustrates the resulting one-dimensional CUF-based model of the TRAC longeron.

A second deployable structure analyzed in this study is a strip obtained by connecting two TRAC longerons with straight battens. Exploiting the capabilities of CUF, this geometrically complex assembly is modeled as a single equivalent beam whose axis lies along the y-direction, with cross-sections defined in the (x, z) plane. Two distinct cross-sections are introduced using Lagrange expansions: one that includes the battens and one that represents only the TRAC longerons. These cross-sections are alternated at the corresponding structural nodes to reproduce the actual geometry of the strip. The modeling concept and the resulting CUF–FEM representation are depicted in Fig. 3(a) and Fig. 3(b), respectively. In this way, the displacement field of the entire strip is evaluated through the combined use of the axial shape functions N_i and the cross-sectional expansion functions F_τ.

The structure analyzed in this study, shown in Fig. 4, is referred to as a *double-strip* because it is assembled from two

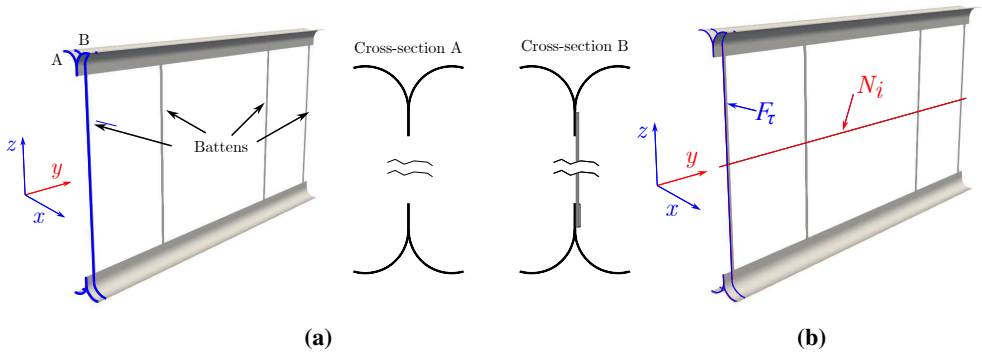

Fig. 3 (a) Geometry of strip composed of two TRAC longerons and connecting battens. (b) CUF-based numerical model of the strip.

identical strip sub-structures connected by a pair of hinges. Each strip consists of two parallel TRAC longerons, which act as the primary load-carrying members, and four straight battens that maintain the relative spacing between the longerons and transfer loads across the structure. When combined through the hinge connections, the two strips form a foldable frame capable of being compactly stowed and subsequently deployed into a stiff, elongated configuration suitable for space applications. The hinges are positioned at the ends of the strips, allowing relative rotation between the sub-structures while preserving the in-plane geometric compatibility of the overall assembly. The reported dimensions correspond to actual physical prototypes employed in an experimental campaign and define the slenderness and local curvature radii that govern both the global deployment kinematics and the onset of local phenomena such as buckling and cross-sectional distortion.

Leveraging the capabilities of the Carrera Unified Formulation (CUF), a refined beam theory is employed to model the entire structure. The double-strip is represented as a CUF-based one-dimensional member whose axis follows the y-direction, while the (x, z) plane describes the cross-section of the TRAC longerons and the battens. Different cross-sectional layouts can be introduced along the axis (for instance, cross-sections including or excluding the battens and hinge regions), enabling the complex geometry of the double-strip to be captured within a unified beam framework. This approach allows local cross-sectional deformations, including those associated with the TRAC geometry, to be consistently coupled with the global motion imposed by the hinge kinematics, without resorting to computationally expensive shell or solid discretizations. Figure 4 illustrates the finite element (FE) mesh adopted along the y-axis. The beam axis is discretized using both B2 (linear, two-node) and B4 (cubic, four-node) Lagrangian elements. Linear B2 elements provide a robust and efficient description in regions characterized by moderately varying deformation fields, whereas cubic B4 elements offer enhanced accuracy where higher curvature of the displacement field is expected, such as in the vicinity of the hinges and load introduction points. The combination of these two element types, within the CUF framework, enables an effective balance between computational cost and accuracy in the double-strip deployment mechanism.

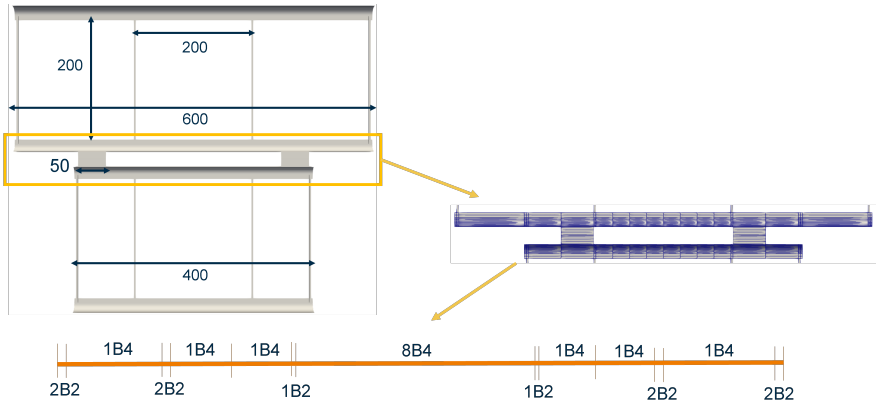

Fig. 4 Mesh discretization for the deployable structure.

A. Strain field and constitutive relations

The stress, $\boldsymbol{\sigma}$, and strain, $\boldsymbol{\epsilon}$, components are collected in vector form as

$$\begin{aligned} \sigma &= \{\sigma_{xx} \;\; \sigma_{yy} \;\; \sigma_{zz} \;\; \sigma_{xz} \;\; \sigma_{yz} \;\; \sigma_{xy}\}^T \\ \epsilon &= \{\epsilon_{xx} \;\; \epsilon_{yy} \;\; \epsilon_{zz} \;\; \epsilon_{xz} \;\; \epsilon_{yz} \;\; \epsilon_{xy}\}^T \end{aligned} \tag{5}$$

The Green–Lagrange strain vector is decomposed into linear and nonlinear parts as

$$\boldsymbol{\epsilon} = \boldsymbol{\epsilon} l + \boldsymbol{\epsilon} nl = (\mathbf{b}l + \mathbf{b}nl), \mathbf{u}, \tag{6}$$

where $\mathbf{b}l$ and $\mathbf{b}nl$ are the 6×3 linear and nonlinear differential operator matrices, respectively, given by

$$\mathbf{b}l = \begin{bmatrix} \partial x & 0 & 0 \\ 0 & \partial_y & 0 \\ 0 & 0 & \partial_z \\ \partial_z & 0 & \partial_x \\ 0 & \partial_z & \partial_y \\ \partial_y & \partial_x & 0 \end{bmatrix}, \qquad \mathbf{b}nl = \begin{bmatrix} \frac{1}{2}(\partial x)^2 & \frac{1}{2}(\partial_x)^2 & \frac{1}{2}(\partial_x)^2 \\ \frac{1}{2}(\partial_y)^2 & \frac{1}{2}(\partial_y)^2 & \frac{1}{2}(\partial_y)^2 \\ \frac{1}{2}(\partial_z)^2 & \frac{1}{2}(\partial_z)^2 & \frac{1}{2}(\partial_z)^2 \\ \partial_x\partial_z & \partial_x\partial_z & \partial_x\partial_z \\ \partial_y\partial_z & \partial_y\partial_z & \partial_y\partial_z \\ \partial_x\partial_y & \partial_x\partial_y & \partial_x\partial_y \end{bmatrix}, \tag{7}$$

with $\partial_\alpha = \partial(\cdot)/\partial\alpha$ for $\alpha = x, y, z$.

Linear elastic, isotropic shell behavior is assumed in this work. The constitutive law therefore takes the form

$$\boldsymbol{\sigma} = \mathbf{C}, \boldsymbol{\epsilon}, \tag{8}$$

where $\mathbf{C}$ is the elastic stiffness matrix of the material [22, 23].

Finally, by inserting the CUF expansion and the FEM interpolation of Eq. (3) into Eq. (6), the strain vector can be written in the algebraic form

$$\boldsymbol{\epsilon} = \left(\mathbf{B}^{\tau i} l + \mathbf{B}^{\tau i} nl\right), \mathbf{q}\tau i, \tag{9}$$

where $\mathbf{q}\tau i$ is the vector collecting the generalized nodal unknowns, and $\mathbf{B}^{\tau i} l$ and $\mathbf{B}^{\tau i} nl$ are the linear and nonlinear algebraic strain–displacement matrices arising from the combined CUF–FEM formulation. Their explicit expressions are not reported here for brevity and can be found in [24].

III. Nonlinear governing equations

The derivation of the geometrically nonlinear governing equations follows the approach presented in [25] and is briefly recalled here for completeness. Starting from the principle of virtual displacements, the equilibrium of the structure can be expressed as

$$\delta L_{\text{int}} = \delta L_{\text{ext}} \tag{10}$$

where δL_{int} and δL_{ext} denote the virtual variation of the internal strain energy and of the external work, respectively, and $\delta(\cdot)$ indicates a virtual variation.

For a body occupying a volume V, the virtual variation of the internal strain energy is written as

$$\delta L_{\text{int}} = \int_{\text{V}} \delta \boldsymbol{\epsilon}^T \boldsymbol{\sigma} \, \text{dV} \tag{11}$$

where $\boldsymbol{\epsilon}$ and $\boldsymbol{\sigma}$ are the strain and stress vectors, respectively. The virtual strain variation, in terms of the generalized displacement parameters $\mathbf{q}_{sj}$ and the linear and nonlinear strain–displacement operators $\mathbf{B}_l^{sj}$ and $\mathbf{B}_{nl}^{sj}$, can be written as

$$\delta\boldsymbol{\epsilon} = \delta((\mathbf{B}_l^{sj} + \mathbf{B}_{nl}^{sj})\mathbf{q}_{sj}) = \delta\mathbf{q}_{sj}^T(\mathbf{B}_l^{sj} + 2\mathbf{B}_{nl}^{sj}) \tag{12}$$

Substituting Eq. (12) into Eq. (11), the internal virtual work can be re-expressed in terms of the generalized displacements

as

$$
\begin{aligned}
\delta L_{\text{int}} &= \delta \mathbf{q}_{sj}^T \int_{\text{V}} (\mathbf{B}_l^{sj} + 2\mathbf{B}_{nl}^{sj})^T \boldsymbol{\sigma} \, \text{dV} = \\
&= \delta \mathbf{q}_{sj}^T \int_{\text{V}} (\mathbf{B}_l^{sj} + 2\mathbf{B}_{nl}^{sj})^T \mathbf{C} (\mathbf{B}_l^{\tau i} + \mathbf{B}_{nl}^{\tau i}) \, \text{dV} \mathbf{q}_{\tau i} = \\
&= \delta \mathbf{q}_{sj}^T \mathbf{K}_0^{ij\tau s} \mathbf{q}_{\tau i} + \delta \mathbf{q}_{sj}^T \mathbf{K}_{lnl}^{ij\tau s} \mathbf{q}_{\tau i} \\
&+ \delta \mathbf{q}_{sj}^T \mathbf{K}_{nll}^{ij\tau s} \mathbf{q}_{\tau i} + \delta \mathbf{q}_{sj}^T \mathbf{K}_{nlnl}^{ij\tau s} \mathbf{q}_{\tau i} \\
&= \delta \mathbf{q}_{sj}^T \mathbf{K}_S^{ij\tau s} \mathbf{q}_{\tau i}
\end{aligned}
\tag{13}
$$

Here, $\mathbf{C}$ is the constitutive matrix, and $\mathbf{K}_0^{ij\tau s}$, $\mathbf{K}_{lnl}^{ij\tau s}$, $\mathbf{K}_{nll}^{ij\tau s}$, and $\mathbf{K}_{nlnl}^{ij\tau s}$ are the linear and nonlinear contributions to the element-level secant stiffness. Their sum defines the *fundamental nucleus* of the secant stiffness matrix,

$$
\mathbf{K}_S^{ij\tau s} = \mathbf{K}_0^{ij\tau s} + \mathbf{K}_{lnl}^{ij\tau s} + \mathbf{K}_{nll}^{ij\tau s} + \mathbf{K}_{nlnl}^{ij\tau s}.
$$

Each $\mathbf{K}_S^{ij\tau s}$ is a 3×3 matrix associated with a given combination of cross-sectional expansion functions (F_τ, F_s) and axial shape functions (N_i, N_j). By looping over the cross-sectional indices $\tau, s = 1, \ldots, M$ and the axial indices $i, j = 1, \ldots, N_n$, the elemental secant stiffness matrix is obtained and then assembled into the global stiffness matrix following the standard FEM procedure [15].

The explicit expressions of the linear and nonlinear contributions to the nucleus are

$$
\begin{aligned}
\mathbf{K}_0^{ij\tau s} &= \int_{\text{V}} (\mathbf{B}_l^{sj})^T \mathbf{C} \mathbf{B}_l^{\tau i} \, \text{dV} \qquad \mathbf{K}_{lnl}^{ij\tau s} = \int_{\text{V}} (\mathbf{B}_l^{sj})^T \mathbf{C} \mathbf{B}_{nl}^{\tau i} \, \text{dV} \\
\mathbf{K}_{nll}^{ij\tau s} &= 2 \int_{\text{V}} (\mathbf{B}_{nl}^{sj})^T \mathbf{C} \mathbf{B}_l^{\tau i} \, \text{dV} \qquad \mathbf{K}_{nlnl}^{ij\tau s} = 2 \int_{\text{V}} (\mathbf{B}_{nl}^{sj})^T \mathbf{C} \mathbf{B}_{nl}^{\tau i} \, \text{dV}
\end{aligned}
\tag{14}
$$

The matrix $\mathbf{K}_S$ obtained from Eq. (13) is, in general, non-symmetric, which may lead to mathematical and computational drawbacks. Several strategies have been proposed in the literature to enforce symmetry of secant or tangent stiffness matrices in nonlinear formulations, see for instance [26–28].

In this work, the symmetric representation introduced in [24] is adopted. It is obtained by reformulating the

contribution of $\mathbf{K}_{nll}^{ij\tau s}$ to the virtual internal work as

$$\begin{aligned} \delta L_{\text{int}nll} &= \int_{\text{V}} \delta\boldsymbol{\epsilon}^T \boldsymbol{\sigma} \, \text{dV} \\ &= \frac{1}{2} \int_{\text{V}} \delta\boldsymbol{\epsilon}_{nl}^T \mathbf{C} \boldsymbol{\epsilon}_l + \delta\boldsymbol{\epsilon}_{nl}^T \boldsymbol{\sigma}_l \, \text{dV} \\ &= \delta\mathbf{q}_{sj}^T (\mathbf{K}_{nll}^{ij\tau s} + \mathbf{K}_{\sigma l}^{ij\tau s}) \mathbf{q}_{\tau i} \end{aligned} \tag{15}$$

where $\boldsymbol{\epsilon}_l$ and $\boldsymbol{\epsilon}_{nl}$ are the linear and nonlinear strain components, $\boldsymbol{\sigma}_l$ is the stress vector associated with the linear strain, and $\mathbf{K}_{\sigma l}^{ij\tau s}$ is an additional matrix arising from this rearrangement.

By combining Eq. (15) with Eq. (13), the complete virtual internal work can be expressed as

$$\delta L_{\text{int}} = \delta\mathbf{q}_{sj}^T (\mathbf{K}_0^{ij\tau s} + \mathbf{K}_{lnl}^{ij\tau s} + \frac{1}{2}\mathbf{K}_{nll}^{ij\tau s} + \frac{1}{2}\mathbf{K}_{\sigma l}^{ij\tau s} + \mathbf{K}_{nlnl}^{ij\tau s}) \mathbf{q}_{\tau i} \tag{16}$$

which corresponds to an expanded, symmetric form of the fundamental nucleus of the secant stiffness matrix.

On the other hand, the external load vector is obtained from the virtual work of the external forces. Omitting intermediate algebraic steps, the contribution of the external loading is written as

$$\delta L_{\text{ext}} = \delta\mathbf{q}_{sj}^T \mathbf{F}_{ext}^{\tau i} \tag{17}$$

The fully assembled global stiffness matrix and external force vector are obtained by looping over the indices i, j, τ and s in the nuclei of Eqs. (16) and (17). Substituting these expressions into Eq. (10) leads to the discrete nonlinear equilibrium equation

$$\mathbf{K}_S \; \mathbf{q} = \mathbf{F}_{ext} \tag{18}$$

Equation (18) represents a system of geometrically nonlinear algebraic equations, which is typically solved by means of an incremental–iterative scheme. In this work, the Newton–Raphson method is employed. The equilibrium equations are then written in residual form as

$$\boldsymbol{\varphi}_{res} \equiv \mathbf{K}_S \; \mathbf{q} - \mathbf{F}_{ext} = 0 \tag{19}$$

where $\boldsymbol{\varphi}_{res}$ is the vector of residual nodal forces. A known solution state $(\mathbf{q}, \mathbf{p})$ is used as a reference to linearize

Eq. (19) by expanding $\boldsymbol{\varphi}_{res}$ in a Taylor series,

$$\boldsymbol{\varphi}_{res}(\mathbf{q}+\delta\mathbf{q},\mathbf{p}+\delta\mathbf{p}) = \boldsymbol{\varphi}_{res}(\mathbf{q},\mathbf{p}) + \frac{\partial\boldsymbol{\varphi}_{res}}{\partial\mathbf{q}}\,\delta\mathbf{q} + \frac{\partial\boldsymbol{\varphi}_{res}}{\partial\mathbf{p}}\,\delta\lambda\,\mathbf{p}_{ref} = 0 \tag{20}$$

where $\dfrac{\partial\boldsymbol{\varphi}_{res}}{\partial\mathbf{q}} = \mathbf{K}_T$ defines the *tangent* stiffness matrix.

The external load is expressed in terms of a reference distribution $\mathbf{p}_{ref}$ and a scalar load factor λ, i.e. $\mathbf{p} = \lambda\,\mathbf{p}_{ref}$. Since λ is unknown, an additional constraint equation is required, involving both $\delta\mathbf{q}$ and $\delta\lambda$. The Newton–Raphson iteration can then be written as

$$\begin{cases} \mathbf{K}_T\,\delta\mathbf{q} = \delta\lambda\,\mathbf{p}_{ref} - \boldsymbol{\varphi}_{res} \\ \\ c(\delta\mathbf{q},\delta\lambda) = 0 \end{cases} \tag{21}$$

In the present work, the condition $c(\delta\mathbf{q},\delta\lambda) = \delta\mathbf{q} = 0$ is adopted, corresponding to a displacement-control strategy. Further details on such procedures can be found in [29–31].

It is worth emphasizing that $\mathbf{K}_T$ is obtained from the linearization of the equilibrium equations [32], which is equivalent to linearizing the virtual internal work of the conservative forces:

$$\delta(\delta L_{\text{int}}) = \int_{\text{V}} \delta(\delta\boldsymbol{\epsilon}^T\boldsymbol{\sigma})\ \text{dV} = \delta\mathbf{q}_{sj}^T\mathbf{K}_T^{ij\tau s}\delta\mathbf{q}_{\tau i} \tag{22}$$

Here, $\mathbf{K}_T^{ij\tau s}$ represents the fundamental nucleus of the tangent stiffness matrix in the CUF–FEM framework [33].

A. Contact formulation

Contact between the two flanges of the TRAC longeron is modeled by a node-to-node penalty formulation explained in [34]. Briefly, the two interacting flanges are idealized as master and slave bodies: for each point on the master surface, a local orthonormal basis is constructed, whose in-plane tangent vectors define the surface directions and whose cross product gives the outward normal vector. The slave surface is then "seen" from each master node through a distance vector, which joins the master point to the closest point on the slave surface. In the CUF–FEM framework, this distance is expressed in terms of the generalized nodal displacements by combining the cross-sectional expansion functions and the axial shape functions. A scalar gap is defined and its sign is used to distinguish between open and closed configurations. When the gap is positive, the two surfaces are separated and no normal reaction is applied. Otherwise, when the gap becomes negative, interpenetration is numerically detected and a penalty spring of stiffness k is activated, generating equal and opposite normal forces on the two nodes and contributing an additional contact force vector and contact stiffness matrix to the global equilibrium equations. The virtual work of these contact forces is written in terms of the generalized displacements and variations, integrated over the contact area, and the resulting contributions are

assembled in the standard way into the global force vector and stiffness matrix so that contact is enforced consistently within the nonlinear CUF–FEM formulation.

In addition to this standard penalty contact treatment, a small hysteresis is introduced in the normal contact law to improve robustness and better represent the physics of the interface. Instead of switching the contact spring on and off exactly at zero gap, two distinct thresholds are defined for each potential contact pair: an activation threshold $g_{on} < 0$ and a release threshold $g_{off} > 0$. When the bodies approach each other, contact is activated as soon as the normal gap falls below g_{on}; once active, the contact remains engaged during unloading and only deactivates when the gap becomes g_{off}. The contact state (open/closed) is thus governed by a history variable that stores whether the pair is currently in contact, and the decision at a given load step depends not only on the instantaneous value of the gap but also on this internal variable. As a result, a narrow hysteretic band is created around the nominal contact boundary: small oscillations of the gap around zero no longer cause rapid, repeated activation and deactivation of the penalty spring. This has two main benefits. Numerically, it suppresses "chattering" of contact constraints and associated spikes in the stiffness matrix, leading to smoother convergence of the Newton–Raphson iterations and more stable solutions in strongly nonlinear configurations. Physically, the resulting force–gap relation exhibits a minor hysteresis loop. Similar hysteretic normal contact laws have been successfully used to model bolted joints and rough dry contacts within finite element formulations, where a penalty-type constitutive relation with memory is introduced to reproduce measured contact hysteresis loops and their associated damping [35, 36].

IV. Numerical Results

The folding simulation sequence consists of three steps:

- **Rotation**: The hinge is constrained and the longer strip is rotated (see Fig. 5(a)). A prescribed rotation is applied to the longerons of the longer strip while the hinge line is clamped, and the rotation is increased quasi-statically to reach the target configuration (see Fig 5(a)).
- **Pinching**: It is performed by applying imposed displacements (see Fig. 5(b)). Once the rotated configuration is reached, opposite kinematic constraints are applied on the lateral edges in order to progressively close the cross-section and promote flange–flange interaction. This "pinching" step mimics the action of a mechanical clamp used in practice to drive the strip toward its stowed geometry. The imposed displacements are again applied quasi-statically, allowing for the development of local bending, contact pressures, and possible snap-through phenomena in a controlled manner.
- **Folding**: The structure is constrained in the middle and rotations are applied at the edges (see Fig. 5(c)). In this final step, the previously pinched longeron is folded about transverse axis located at mid-span, while suitable boundary conditions are enforced to prevent rigid-body motions. Rotations are prescribed at the strip ends, driving the system toward a compact configuration and inducing large overall curvatures and significant redistribution

of internal forces. This step is representative of the actual stowage process of the deployable member and is particularly demanding from the numerical standpoint due to the combination of large displacements and contact nonlinearities.

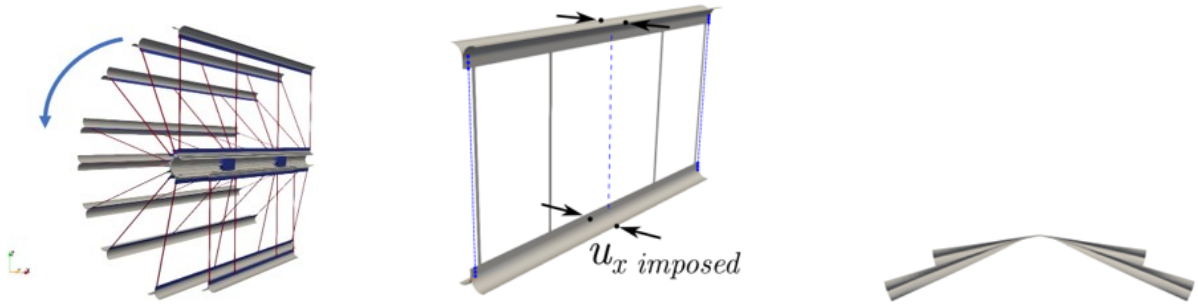

Fig. 5 Simulation sequence.

The simulation is carried out for two structural configurations: (i) the double-strip longeron introduced in the previous sections and (ii) a more complex assembly comprising four interacting strips. The former configuration is used as a reference case, enabling a clear interpretation of the nonlinear response and of the contact interaction within a single longeron pair. The latter configuration is closer to real SSPP structure, as it represents a full quadrant [37], with four strips arranged according to the actual cross-sectional layout. For the four-strip quadrant, the same CUF-based modeling strategy is adopted, namely the entire structure is represented by a single 1D beam finite element as reported in Fig. 6, whose cross-section accounts for the geometry and mutual interaction of the four strips.

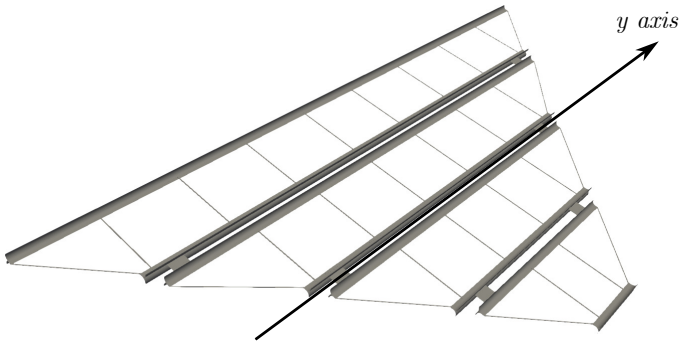

Fig. 6 Model of the elastically foldable flat array.

This choice highlights the capability of the proposed formulation to model a complex three-dimensional architecture into a reduced-order 1D model while retaining the essential mechanical features. In the present study, only the *Rotation* step is simulated for this more realistic structure, with the objective of assessing the global response and the influence of the additional strips on stiffness and deformation patterns. The *Pinching* and *Folding* steps for the full quadrant

will be addressed in dedicated future studies, where a detailed investigation of multi-strip contact and fully folded configurations will be performed.

V. Double strip

The double-strip structure is analyzed first. In the initial step, only the global rotation about the central hinge is prescribed, and the corresponding final configuration is shown in Fig. 7. The number of DOF is equal to 170,904.

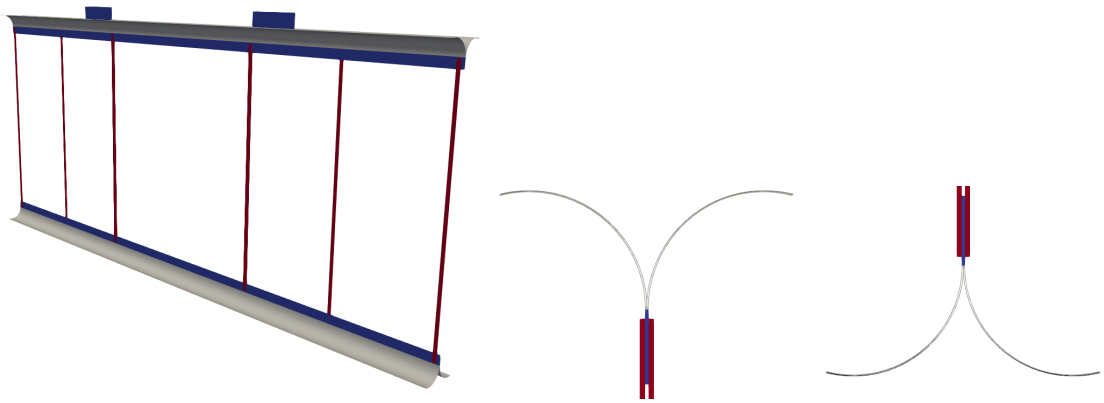

(a) **(b)** **(c)**

Fig. 7 Simulation sequence. TRAcs contact modeling (a and b).

During this purely kinematic rotation, the finite element model would naturally lead to interpenetration between adjacent longerons. To avoid the large number of local contact events that this would generate, the contact between neighbouring longerons is intentionally not activated in this step. Such contacts would drastically increase the computational cost without providing a meaningful improvement in the accuracy of the global rotational response. For this reason, the only active contact in the first step is defined between the two webs, which acts as a mechanical stop and allows the instant at which the prescribed overall rotation is attained to be unambiguously identified. This modeling strategy strongly reduces both the number and the magnitude of contact forces and, consequently, the overall computational time. In this first analysis stage, the absence of local contact constraints between adjacent TRAC longerons and the lack of local deformations imply that the double strip essentially behaves as two rigid bodies rotating about the hinge. In an ideal rigid-body motion, the internal strain energy should remain identically zero. The numerical results confirm this expectation: the internal energy remains negligibly small throughout the entire rotation process, with only minor numerical fluctuations, thus confirming the rigid-body nature of the motion. In the second step of the analysis, corresponding to the pinching, the contact between adjacent TRAC longerons is activated; the final configuration for this step is reported in Fig. 8. As illustrated in Fig. 5, two pairs of imposed displacements are prescribed at the ends of the two flanges of the same TRAC. These displacements locally flatten the cross-section and reduce the bending stiffness within a narrow region of the strip. The resulting locally compliant hinge is essential to promote and control

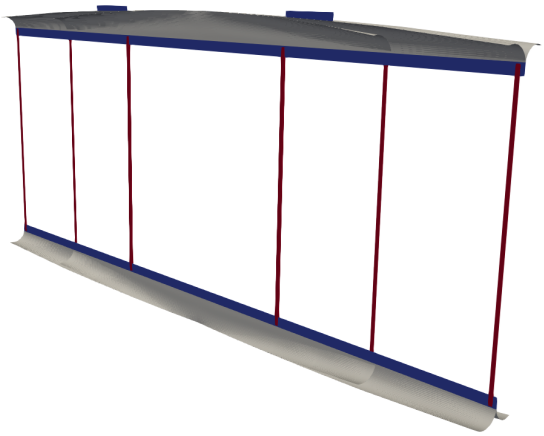

Fig. 8 Pinched rotated double strip.

the subsequent folding of the structure about this pinched zone. In contrast to the first step, the structure now undergoes significant local deformation and, as a consequence, the internal strain energy increases as the imposed displacements grow. This trend clearly reflects the elastic energy that is being stored in the pinched region due to the local modification of the TRAC geometry. Finally, in the third step, the actual folding of the double strip is simulated. The structure is bent about the previously created compliant zone until a target folding rotation of 90° is reached, as shown in Fig. 9. During this stage, the internal energy continues to increase, since additional elastic deformation accumulates both in the pinched region and in the neighbouring portions of the longerons. The internal energy at the end of the folding step represents the amount of strain energy stored in the structure, which will act as the driving mechanism for the subsequent deployment. The deployment phase itself is not addressed in the present work and will be the subject of dedicated future studies.

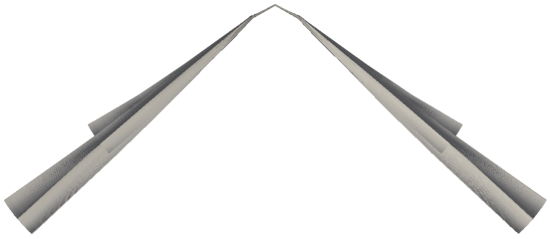

Fig. 9 Configuration corresponding to folding angle of 90°.

VI. Full quadrant structure

The response of a full quadrant structure is now investigated. The geometry of the quadrant is taken from [38] and the model is reported in Fig. 10. The numerical model is built entirely with 1D beam finite elements, resulting in a total of 267,156 degrees of freedom, which allows for an accurate description of both the global kinematics and the local deformation modes of the structural members. The same rotation sequence adopted for the double-strip configuration is now applied to the full quadrant.

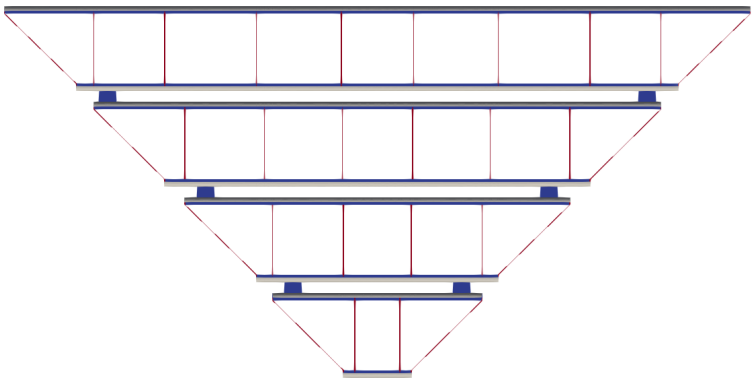

Fig. 10 Model of elastically foldable flat array .

Finally, Fig. 11 shows the rotation of the full quadrant. From a numerical standpoint, the evolution of the internal energy

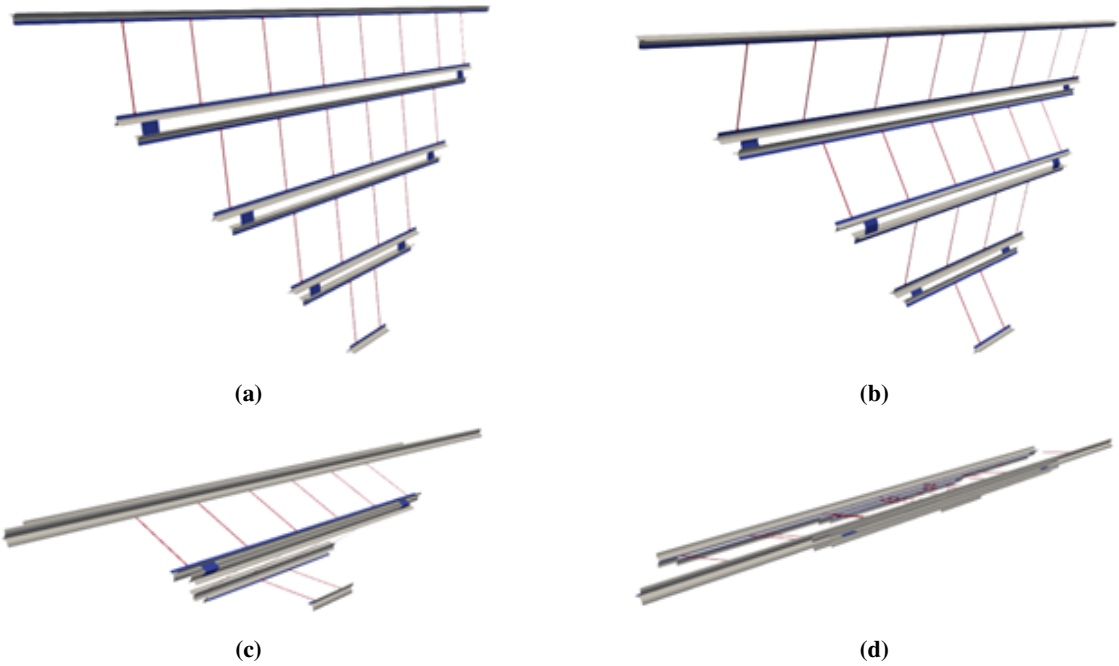

(a) **(b)**

(c) **(d)**

Fig. 11 Rotation of full quadrant of SSPP structure.

during the rotation is particularly informative. The internal energy remains essentially constant throughout the rotation

step, indicating that the motion is very close to a rigid-body-like rotation, in full analogy with what was observed for the double-strip rotation.

VII. Conclusion

This paper has presented a refined one-dimensional finite element framework for simulating the folding of elastically foldable flat arrays based on Triangular Rollable and Collapsible (TRAC) longerons. The formulation builds on the Carrera Unified Formulation (CUF), in which the three-dimensional kinematics are decomposed into axial and cross-sectional parts, enabling higher-order cross-sectional behavior to be represented through nine-point Lagrange expansions while retaining a one-dimensional beam description along the array span. By alternating appropriate cross-sections, the same CUF beam model is used to represent single TRAC longerons, strips with battens, and a full double-strip mechanism assembled through hinges, so that the entire array is modeled as a single, geometrically exact beam element chain with a modest number of degrees of freedom.

Geometrically nonlinear effects are included through Green–Lagrange strains and a unified derivation of the secant and tangent stiffness matrices, for which a symmetric fundamental nucleus is constructed and solved via an implicit quasi-static Newton–Raphson scheme under displacement control. Contact between the flanges is treated through a node-to-node penalty formulation embedded in the CUF–FEM framework, and a small hysteresis band is introduced in the normal contact law to eliminate chattering and improve numerical robustness while better reflecting the dissipative, history-dependent behavior of real interfaces.

The resulting methodology provides a computationally efficient yet high-fidelity tool for studying the complex kinematics of rotation and folding in TRAC-based arrays and offers a suitable foundation for future parametric studies, design optimization, and extension to dynamic loading conditions and experimentally validated models of large, space-deployable structures.

Acknowledgments

This research was carried out with financial support from the Caltech Space Solar Power Project and is part of the project NOVITAS, funded by the European Union's Horizon Europe research and innovation program under the Marie Sklodowska-Curie grant agreement No 101059825.

References

[1] Marshall, M. A., and Pellegrino, S., "Slew maneuver constraints for agile flexible spacecraft," *Journal of Guidance, Control, and Dynamics*, Vol. 46, No. 12, 2023, pp. 2300–2314.

[2] Santiago-Prowald, J., and Drioli, L. S., "Space environment and materials," *Space antenna handbook*, 2012, pp. 106–132.

[3] Banik, J., and Murphey, T., "Performance validation of the triangular rollable and collapsible mast," 2010.

[4] Murphey, T. W., and Banik, J., "Triangular rollable and collapsible boom," , 2011. USA Patent 7,895,795.

[5] Johnson, L., Whorton, M., Heaton, A., Pinson, R., Laue, G., and Adams, C., "NanoSail-D: A solar sail demonstration mission," *Acta Astronautica*, Vol. 68, No. 5-6, 2011, pp. 571–575.

[6] Leclerc, C., Wilson, L. L., Bessa, M. A., and Pellegrino, S., "Characterization of ultra-thin composite triangular rollable and collapsible booms," *4th AIAA Spacecraft Structures Conference*, 2017, p. 0172.

[7] Arya, M., Lee, N., and Pellegrino, S., "Ultralight structures for space solar power satellites," *3rd AIAA Spacecraft Structures Conference*, 2016, p. 1950.

[8] Pappa, R. S., Lassiter, J. O., and Ross, B. P., "Structural dynamics experimental activities in ultralightweight and inflatable space structures," *Journal of Spacecraft and Rockets*, Vol. 40, No. 1, 2003, pp. 15–23.

[9] Pellegrino, S., "Deployable structures in engineering," *Deployable Structures*, Springer, 2001, pp. 1–35.

[10] Carmi, M. O., Cooley, S., and Pellegrino, S., "Effects of Varying Geometric Design Parameters on the Stability of Deployable Thin-Shell Composite Space Structures," *AIAA SCITECH 2024 Forum*, 2024, p. 0606.

[11] Oberst, S., and Tuttle, S., "Nonlinear dynamics of thin-walled elastic structures for applications in space," *Mechanical Systems and Signal Processing*, Vol. 110, 2018, pp. 469–484.

[12] Guckenheimer, J., and Holmes, P., *Nonlinear oscillations, dynamical systems, and bifurcations of vector fields*, Vol. 42, Springer Science & Business Media, 2013.

[13] Zhang, X., Nie, R., Chen, Y., and He, B., "Deployable structures: structural design and static/dynamic analysis," *Journal of Elasticity*, 2021, pp. 1–37.

[14] Teodorescu-Draghicescu, H., Stanciu, A., Vlase, S., Scutaru, L., Calin, M., Serbina, L., et al., "Finite element method analysis of some fibre-reinforced composite laminates," *Optoelectron. Adv. Mater. Rapid Commun*, Vol. 5, No. 7, 2011, pp. 782–785.

[15] Carrera, E., Cinefra, M., Petrolo, M., and Zappino, E., *Finite element analysis of structures through unified formulation*, John Wiley & Sons, Hoboken, New Jersey, USA, 2014.

[16] Carrera, E., Pagani, A., and Augello, R., "Evaluation of geometrically nonlinear effects due to large cross-sectional deformations of compact and shell-like structures," *Mechanics of Advanced Materials and Structures*, Vol. 27, No. 14, 2020, pp. 1269–1277.

[17] Pagani, A., Augello, R., and Carrera, E., "Numerical simulation of deployable ultra-thin composite shell structures for space applications and comparison with experiments," *Mechanics of Advanced Materials and Structures*, Vol. 30, No. 8, 2023, pp. 1591–1603.

[18] Augello, R., and Pellegrino, S., "Vibration Damping of Thin-Shell Deployable Structures Through Local Buckling," *AIAA SCITECH 2025 Forum*, 2025, p. 0693.

[19] Augello, R., Carrera, E., Pagani, A., and Pellegrino, S., "Folding simulation of TRAC longerons via unified one-dimensional finite elements," *Materials Research Proceedings*, Vol. 37, 2024.

[20] Carrera, E., and Petrolo, M., "Refined one-dimensional formulations for laminated structure analysis," *AIAA Journal*, Vol. 50, No. 1, 2012, pp. 176–189. https://doi.org/10.2514/1.J051219.

[21] Carrera, E., and Petrolo, M., "Refined beam elements with only displacement variables and plate/shell capabilities," *Meccanica*, Vol. 47, 2012, pp. 537–556. https://doi.org/10.1007/s11012-011-9466-5.

[22] Bathe, K.-J., *Finite element procedures*, Klaus-Jurgen Bathe, 2006.

[23] Hughes, T. J. R., *The finite element method: linear static and dynamic finite element analysis*, Courier Corporation, 2012.

[24] Pagani, A., and Carrera, E., "Unified formulation of geometrically nonlinear refined beam theories," *Mechanics of Advanced Materials and Structures*, Vol. 25, No. 1, 2018, pp. 15–31.

[25] Pagani, A., and Carrera, E., "Large-deflection and post-buckling analyses of laminated composite beams by Carrera Unified Formulation," *Composite Structures*, Vol. 170, 2017, pp. 40–52. https://doi.org/10.1016/j.compstruct.2017.03.008.

[26] Oñate, E., "On the derivation and possibilities of the secant stiffness matrix for non linear finite element analysis," *Computational Mechanics*, Vol. 15, No. 6, 1995, pp. 572–593. https://doi.org/10.1007/BF00350269.

[27] Badawi, M., and Cusens, A. R., "Symmetry of the stiffness matrices for geometrically non-linear analysis," *Communications in Applied Numerical Methods*, Vol. 8, No. 2, 1992, pp. 135–140. https://doi.org/10.1002/cnm.1630080209.

[28] Morán, A., Oñate, E., and Miquel, J., "A general procedure for deriving symmetric expressions for the secant and tangent stiffness matrices in finite element analysis," *International Journal for Numerical Methods in Engineering*, Vol. 42, No. 2, 1998, pp. 219–236. https://doi.org/10.1002/(SICI)1097-0207(19980530)42:2<219::AID-NME355>3.0.CO;2-E.

[29] Reddy, J., *An Introduction to Nonlinear Finite Element Analysis Second Edition: with applications to heat transfer, fluid mechanics, and solid mechanics*, Oxford University Press, Oxford, 2014.

[30] Carrera, E., "A study on arc-length-type methods and their operation failures illustrated by a simple model," *Computers & Structures*, Vol. 50, No. 2, 1994, pp. 217–229. https://doi.org/https://doi.org/10.1016/0045-7949(94)90297-6.

[31] Crisfield, M., *Non-linear finite element analysis of solids and structures*, John Wiley $ Sons, Chichester, England, 1991.

[32] Zienkiewicz, O. C., and Taylor, R. L., *The finite element method for solid and structural mechanics*, Elsevier, 2005.

[33] Carrera, E., "Theories and finite elements for multilayered plates and shells: a unified compact formulation with numerical assessment and benchmarking," *Archives of Computational Methods in Engineering*, Vol. 10, 2003, pp. 215–296. https://doi.org/10.1007/BF02736224.

[34] Augello, R., and Pellegrino, S., "Implicit Folding Simulation of Ultrathin Shells Using Refined One-Dimensional Finite Elements," *AIAA Journal*, 2025, pp. 1–11.

[35] Yuan, D., Wang, D., and Wan, Q., "Modeling for hysteresis contact behavior of bolted joint interfaces with memory effect penalty constitution," *Machines*, Vol. 12, No. 3, 2024, p. 190.

[36] Armand, J., Pesaresi, L., Salles, L., Wong, C., and Schwingshackl, C. W., "A modelling approach for the nonlinear dynamics of assembled structures undergoing fretting wear," *Proceedings of the Royal Society A*, Vol. 475, No. 2223, 2019, p. 20180731.

[37] Gdoutos, E., Sommer, C. F., Truong, A., Wen, A., Pedivellano, A., Ubamanyu, K., Madonna, R. G., and Pellegrino, S., "Development of the Deployable on-Orbit ultraLight Composite Experiment (DOLCE) for the space solar power project demonstration mission," *AIAA SciTech 2022 Forum*, 2022, p. 1266.

[38] Kechri, M., Mallikarachchi, C., Truong, A., Sauder, J. F., and Pellegrino, S., "Novel Structurally Connected Architecture for Controlled Deployment of Elastically Foldable Flat Arrays," *AIAA Scitech 2025 Forum*, 2025, p. 0813.